Chapter 16
Aeroelastic Simulation of Flexible Membrane Wings based on Multibody System Dynamics

Jeroen Breukels, Roland Schmehl, Wubbo Ockels

Abstract The chapter describes a simulation framework for flexible membrane wings based on multibody system dynamics. It is intended for applications employing kites, parachutes or parasails with an inflated tubular support structure. The tube structure is discretized by an assembly of rigid bodies connected by universal joints and torsion springs. The canopy of the wing is partitioned into spanwise sections, each represented by a central chordline which is discretized by hinged rigid line elements. The canopy is modeled by a crosswise arrangement of spring-damper elements connecting these joints. The distributed loading of the wing structure is defined in terms of discrete aerodynamic forces. Acting on the joints, these forces are formulated per wing section as functions of local angle of attack, airfoil thickness and camber. The presented load model is the result of a comprehensive computational fluid dynamic analysis, covering the complete operational spectrum of the wing. The approach captures the two-way coupling of structural dynamics and aerodynamics. It is implemented as a toolbox within the commercial software package MSC ADAMS. For validation, the model is compared to existing wind tunnel data of a similar sail wing.

16.1 Introduction

In contrast to rigid wings, flexible membrane wings deform substantially during flight. Since the fabric material has an insignificant bending stiffness, this type of wing is typically designed as a tensile membrane structure, incorporating a bridle line system and an inflatable support structure. Leading Edge Inflatable (LEI) tube kites, for example, employ a pressurized tubular frame which is attached to the lift-generating canopy. Another example are ram-air parafoils which use a dual skin with

Jeroen Breukels · Roland Schmehl (✉) · Wubbo Ockels
Delft University of Technology, Faculty of Aerospace Engineering, Kluyverweg 1, 2629HS Delft, The Netherlands, e-mail: r.schmehl@tudelft.nl

a cell structure that is inflated by the flow pressure on the leading edge. Because of the low weight of the fabric material the inertial forces are generally low and the shape of the wing is determined by the force equilibrium between the external aerodynamic and the internal aerostatic load distributions on the one hand, and the tensile and shear forces in the membrane fabric and bridle lines on the other hand.

The aerodynamics and structural dynamics are strongly coupled and constitute a challenging Fluid-Structure Interaction (FSI) problem. Large-scale deformations, such as spanwise torsion and bending, affect the flow around the wing. As the wing is proceeding on its flight trajectory, the boundary conditions of the FSI problem are continuously changing. However, the time scales of these processes are much larger than the aerodynamic time scale and, as consequence, the aerodynamic wing loading can be regarded as quasi-steady.

The flow around a LEI tube kite and the induced deformation of the canopy is very similar to a flexible sail wing. The main difference is the much lower spanwise deformation of the sail wing due to the mast. Flexible sail wings have been subject to extensive research and development for more than half a century [14]. The aerodynamic characteristics of two-dimensional flexible airfoils or sails without a Leading Edge (LE) tube were investigated by [9] employing thin-airfoil theory to obtain the deflection of the camber line as a function of angle of attack. The study predicted the existence of stable wing shapes without a stagnation point. Experimental results partly confirmed this and discrepancies were attributed to fabric porosity and boundary-layer separation, effects that were not accounted for in the theoretical model. A comparable research was published by [15].

Subsequent studies focused on the aerodynamic characteristics of two full-scale models with double membrane airfoils of different aspect ratios [6, 7]. Wind tunnel tests were performed to analyze lift and drag, static longitudinal and lateral stability and lateral control, and it was concluded that sail wings can achieve lift-to-drag ratios comparable to these of a conventional rigid wing. At low angles of attack, the sail wing exhibited unusually steep slopes of the lift curve and, interestingly, the shape of the leading edge nose only had a small effect on the characteristics of the wing [7]. A round leading edge resulted in slightly higher lift coefficients but had a lower lift-to-drag ratio.

The low speed aerodynamic characteristics of a two-dimensional sail wing were investigated experimentally by [1, 2], assessing the influence of an adjustable slack of sail. The study included a numerical model for estimating the performance of both slightly and highly cambered double membrane airfoils. A prominent conclusion was that the sail wing achieved a higher maximum lift-to-drag ratio than the rigid reference wing. The higher ratio was attributed to the higher lift associated with the increased camber and not due to a lower drag. An extensive research into sail wings was presented by [8], including a comparison between different sail wing configurations. Confirming prior findings, the study showed that sail wings are competitive to conventional rigid wings, especially in low speed applications. Next to the advantage of variable camber, it was concluded that sail wings exhibit a fairly slow rise in drag coefficient, and consequently a slow decrease in lift-to-drag ratio with increasing values of the lift coefficient. Previous research further showed that dou-

ble membrane airfoils achieve a maximum lift-to-drag ratio roughly twice of that of single membrane airfoils.

This chapter presents a computational approach for the aeroelastic simulation of a flexible single-membrane wing, such as a LEI tube kite. The focus is on the aerodynamic load model and the fluid-structure coupling algorithm. Details on the structural model are omitted and the reader is referred to [4, 5]. The aerodynamic load model has also been used within a Finite-Element analysis of kite deformation [3]. The aim of the framework project is to develop an intuitive engineering tool for the design of kites which can be used to quickly assess different wing designs before moving to the prototype phase. Currently, kite design is still an experience-driven process and mainly based on empirical data. In general, many prototypes have to be built and evaluated in trial-and-error iterations. The recent industrial application of kites for energy generation [11] and ship propulsion [10] motivates a more systematic engineering approach to avoid excessive prototyping.

16.2 Computational approach

The computational approach can be subdivided into two distinct components: the multibody system model of the flexible wing and the quasi-steady aerodynamic load model. This section outlines the structural and aerodynamic models and the implementation of the two-way coupling mechanism.

The canopy of the wing is supported by an inflated tubular frame consisting of a leading edge tube with attached strut tubes. This frame is discretized as a multibody system. Universal joints are used to connect two neighboring rigid bodies. This type of joint provides two rotational degrees of freedom and constrains the relative axial rotation of the two neighboring bodies. To account for the bending stiffness of the pressurized tubes, torsion springs are applied in the two rotational degrees of freedom per joint. The spring stiffness is determined experimentally and formulated as function of tube geometry, inflation pressure and material properties.

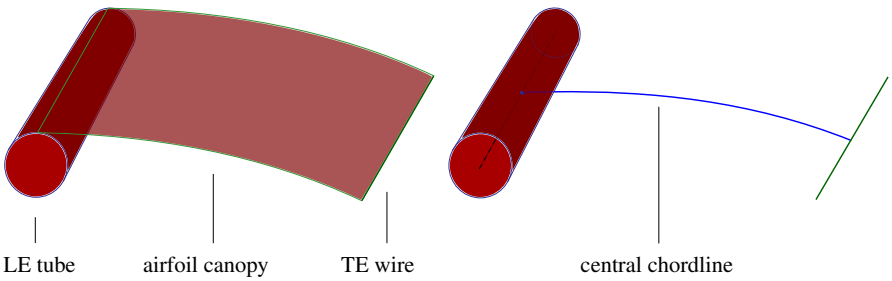

Fig. 16.1 Wing section (left) and spanwise discretization of the canopy by central chordlines (right)

The canopy is partitioned into spanwise sections, each represented by a central chordline, as illustrated in Fig. 16.1. Each chordline is discretized as a chain of five rigid line elements connecting the leading edge with the trailing edge of the wing. The line elements are connected by universal joints. Because the fabric material has an insignificant bending stiffness, these joints allow free rotation without inducing a reaction moment. The material behavior of the fabric membrane is modeled by a network of crosswise spring elements which is attached to the joints of the discretized chordline. The stiffness of theses spring elements is related to the shear modulus of the fabric membrane. Wing designs generally incorporate a trailing edge, which is modeled by additional spring elements. Fig. 16.2 shows the structural model of a representative wing.

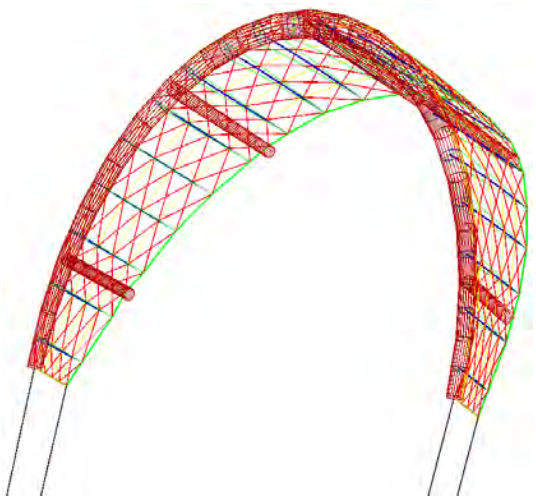

Fig. 16.2 The multibody system representation of the tethered flexible wing. This specific design uses five strut tubes which are attached to the arc-shaped leading edge tube. The canopy is represented by 19 chordlines (blue) and an attached network of crosswise spring elements. The trailing edge wire (green) is modeled by spring elements. The wing is bridled by four lines. The two front lines are the power lines which transfer the major part of the aerodynamic forces. The two rear lines are used for steering and depowering of the wing.

The resultant lift force of a wing is the result of the different pressure distributions on the upper and lower surfaces. The discrete representation of this distributed surface loading is aligned with the canopy model described above, i.e. the nodes of the aerodynamic surface mesh are the joints on the chordlines. Figure 16.1 shows how the aerodynamic force vectors are applied on the five joints per chordline.

The aerodynamic surface load is defined per wing section as function of the local angle of attack, the airfoil thickness and its camber. This surface load data is the result of a comprehensive computational fluid dynamic analysis, covering the complete operational spectrum of the wing. Quasi-steady aerodynamics is a central assumption of this analysis. The correlation framework is described in Sect. 16.3.

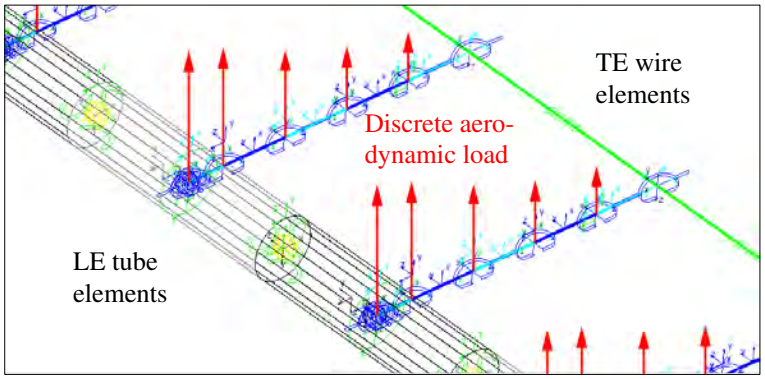

Fig. 16.3 The inflatable membrane wing model showing the chord wise wire elements

16.3 Aerodynamic load model

As was stated in the previous section, the aerodynamic properties are introduced through a set of algorithms which take into account a number of parameters to obtain the local lift, drag and moment coefficients. These input parameters are camber, angle of attack and airfoil thickness. The camber affects the the flow around the wing in a major way and thus has a substantial effect on the characteristics of the wing. The angle of attack is measured locally for every wing section, taking into account the apparent wind velocity and the flexure of the trailing edge wire in vertical direction (body axis). The airfoil thickness introduces the effect of tube radius and the changes in chord length due to the flexure of the trailing edge wire in horizontal direction (body axis). When the trailing edge wire moves towards the leading edge, the chord length is reduced and the camber increases. For the wing types modeled here, this equals to a subsequent increase of the airfoil thickness measured in percentage of the chord length.

In order for the model to use the correct aerodynamic coefficients, an algorithm is required which produces these coefficients as a function of aforementioned camber, angle of attack and airfoil thickness. Previous research by [2, 9, 12, 15] yielded rudimentary numerical models. However, its application within the scope of this simulation proved to be difficult for a number of reasons. None of the models was suited for either the type of wings simulated or proved to be too complicated, substantially slowing down the simulation. Consequently, an approach using polynomial fitting was employed. The data of airfoils of varying thicknesses and cambers is obtained through a computational fluid dynamics (CFD) analysis. Figure 16.4 shows a schematic representation of the aerodynamic model.

It was also attempted to determine surface loading data using specialized aerodynamic analysis software such as XFOIL. However, these exploratory attempts indicated that the separated flow and the associated increased turbulence levels at higher angles of attack yielded only poor results. As was stated earlier, the algorithm for the aerodynamic coefficients determines the aerodynamic properties of

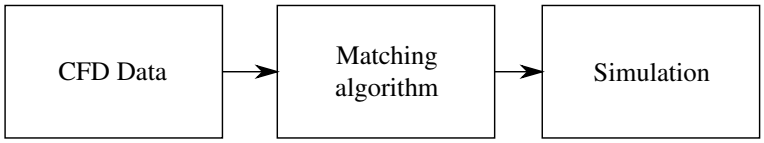

Fig. 16.4 A schematic representation of the aerodynamic model

the simulated wing. Therefore, this algorithm is where characteristics such as single or double membrane, leading edge nose shape and fabric roughness effects on the boundary layer can be found. The different wing configurations exist within the simulation as different aerodynamic coefficient algorithm packages which can be selected by the user. The type of wing discussed in this paper is a single membrane airfoil with a circular leading edge tube. This airfoil is most commonly used in surf kites and functions as a base for further investigations. The CFD analysis was performed on three sets of airfoils with 15, 20 and 25% thicknesses. The airfoils within each set ranged in camber from 0 to 12%. The location of the maximum camber was estimated to lay at 30% if the chord. This value was chosen based on measurements done in [1, 2]. In reality, the location of maximum camber varies somewhat with varying angle of attack. For the purpose of this approximation, it was deemed acceptable to assume the location of camber to be constant. The airfoils were designed by fitting a spline from the trailing edge through the maximum camber point at 30% of the chord to a point on the circular leading edge which is tangent to the arriving spline. To obtain the airfoil polars, a two-dimensional grid was created. Figure 16.5 shows the grid of a 20% thick airfoil with a 4% camber.

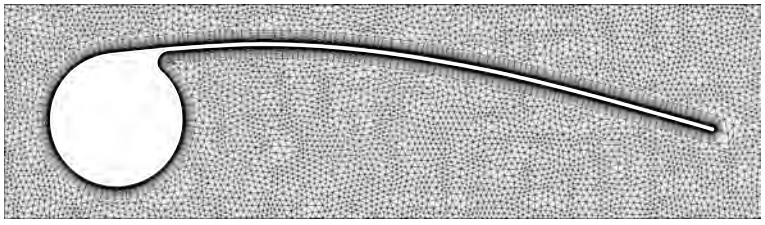

Fig. 16.5 The CFD grid used for determination of aerodynamic coefficients

The analysis is based on an airfoil with a chord of 1m. Around the airfoil there is a 20-cell thick boundary layer which amounts to an absolute thickness of 18mm. The airfoil is placed in a density box with a maximum cell size of 10mm. The outer edge of the grid is a box of 10m long and 8m high. The maximum cell size is 50mm at the outer edges of the grid. The grid model was imported into Fluent from the ICEM mesh generator. The left end and bottom of the outer box is defined as a pressure inlet and the right side and top of the outer box is defined as a pressure outlet. The solver was configured as pressure-based, steady and two-dimensional with a Green-Gauss node based gradient option. For the viscous effects a K-Omega SST

model was chosen incorporating transitional flows. For the solution, the SIMPLEC pressure-velocity coupling was chosen, as well as a second order discretization of pressure, momentum and turbulent kinetic energy.

The turbulent dissipation rate was left on first order. Calculations were done with under-relaxation factors of 0.5 for pressure, 0.7 for momentum, 0.7 for turbulent kinetic energy and 0.7 for turbulent dissipation rate. The case was iterated for angles of attack ranging from 0 to 25° and aerodynamic coefficients were recorded for each angle of attack step. As an example, Fig. 16.6 shows the turbulence intensity around the airfoil for 0, 8 and 12° of angle of attack.

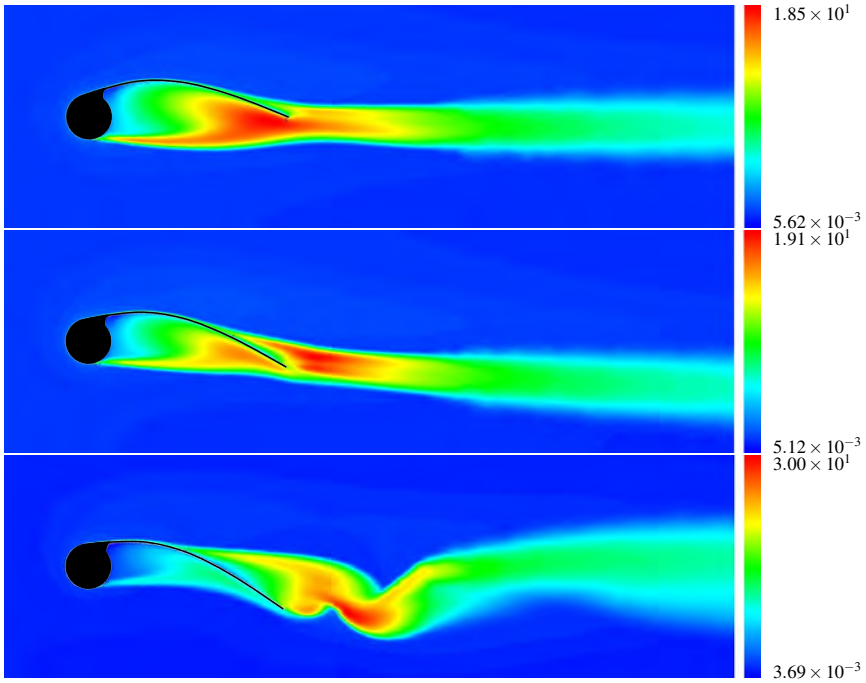

Fig. 16.6 Computed turbulence intensity at angles of attack of 0° (top), 8° (middle) and 12° (bottom)

As can be seen in Fig. 16.6 the airfoil is close to stall at 12° angle of attack. The plot shows an extended area of separated flow with increased turbulence levels at the top surface of the airfoil. It is important to note that the steady flow analysis case does not converge beyond stall. Unsteady analysis of these cases revealed unsteady vortex shedding. From Fig. 16.6 it is further apparent that the lack of a lower membrane inevitably leads to flow separation from the leading edge tube, even at low angles of attack. This is the reason why potential flow-based methods such as XFOIL produce questionable results. The panel-code implemented in XFOIL is unable to cope with such nonlinearities.

For all large number of combinations of different airfoil thicknesses and cambers, the aerodynamic coefficients were plotted against angle of attack. Figure 16.7 shows the lift and drag coefficients for the 15% thick sail wing at different values of camber.

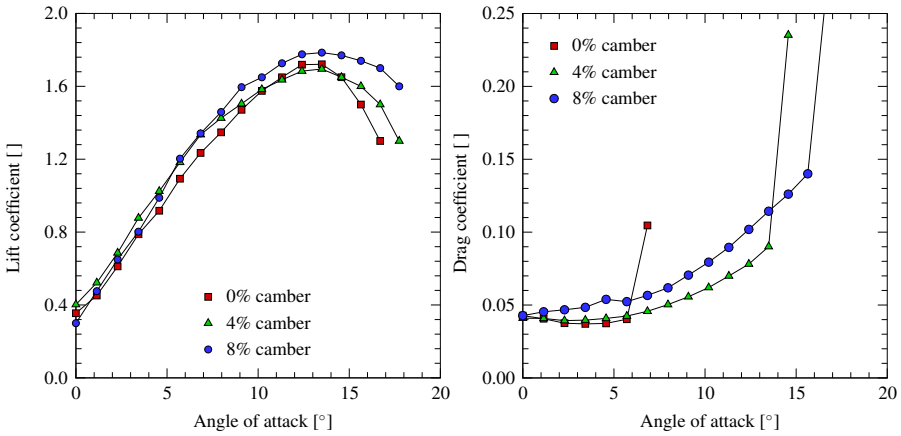

Fig. 16.7 Computed lift (left) and drag (right) curves for a 15% thick sail wing airfoil.

Figure 16.7 (left) clearly shows an increasing lift coefficient with increasing camber. Also, the zero lift angle of attack becomes more and more negative. Higher cambered airfoils show a higher maximum lift coefficient and a more benign stall behavior. However, for the large range of camber values given here, the change of the curve in Fig. 16.7 (left) seems small. For conventional airfoils a larger change can be expected. But the single membrane airfoil differs greatly from a conventional airfoil. As can be seen in Fig. 16.6, even at low angles of attack there is a significant turbulent area on the lower side of the airfoil. The relatively small change in Cl-alpha curve with increased camber is further substantiated by the measurements of [1] which also show a relatively small change with increased camber. Figure 16.7 (right) shows the drag of the same airfoil with angle of attack.

Increasing camber shows an increase in drag on the profile, especially at higher angles of attack. The plot also shows that the 0% cambered airfoil stalls early at an angle of attack of 7°. Such a flat plate shaped airfoil exhibits poor aerodynamic qualities. Figure 16.8 shows the moment coefficient curves of the same airfoil.

Again, one can see that a change in camber has drastic effects. The moment coefficient rapidly becomes more negative with increasing camber. Because of the highly flexible nature of the wing, the camber is closely linked to the pressure difference between the top side and the bottom side of the airfoil. During flight, one can expect to see a range of cambers occurring with all the differences in aerodynamic performance that Figs. 16.7 and 16.8 indicate. In the previous section it was shown how the camber flexibility was simulated from a structural point of view. In order to have the correct aerodynamic performance to go with the flexible wing, an algorithm is

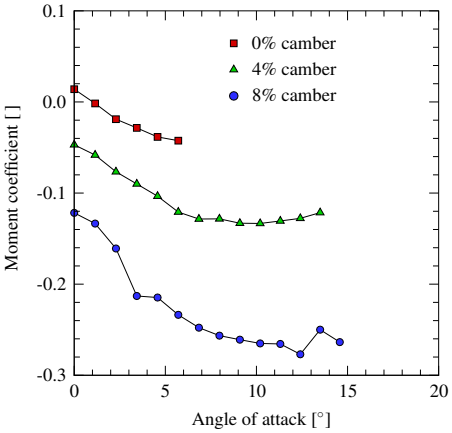

Fig. 16.8 Computed aerodynamic moment curves for a 15% thick sail wing airfoil.

devised which looks at the momentary airfoil thickness, camber and angle of attack and gives a lift, drag and moment coefficient to match that particular configuration. In order to approximate the lift curve with respect to angle of attack, a third order polynomial is chosen. The characteristic shape of the Cl-alpha curve between -20 and 20° is such that the choice for a third order polynomial is deemed to be a good starting point for the approximation. For the lift coefficient as a function of angle of attack, we write:

$$C_l = \gamma_1 \alpha^3 + \gamma_2 \alpha^2 + \gamma_3 \alpha + \gamma_4 \tag{16.1}$$

This yields four coefficients γ_1 through γ_4 which can be approximated using a first order polynomial as a function of camber κ.

$$\gamma_1 = S_1 \kappa + S_2 \tag{16.2a}$$
$$\gamma_2 = S_3 \kappa + S_4 \tag{16.2b}$$
$$\gamma_3 = S_5 \kappa + S_6 \tag{16.2c}$$
$$\gamma_4 = S_6 \kappa + S_8 \tag{16.2d}$$

The first order polynomial was chosen here because, once plotted, the data appeared to fall onto a straight line. Therefore, a first order polynomial was deemed as a good starting point. From the Eqns. (16.2) a new set of coefficients S_1 through S_8 is obtained. The numerical values of these coefficients are plotted as a function of airfoil thickness t. The resulting curves showed a parabolic characteristic, and therefore a second order polynomial was chosen as an initial attempt to approximate this relation:

$$S_1 = C_1 t^2 + C_2 t + C_3 \tag{16.3a}$$
$$S_2 = C_4 t^2 + C_5 t + C_6 \tag{16.3b}$$
$$S_3 = C_7 t^2 + C_8 t + C_9 \tag{16.3c}$$
$$S_4 = C_{10} t^2 + C_{11} t + C_{12} \tag{16.3d}$$
$$S_5 = C_{13} t^2 + C_{14} t + C_{15} \tag{16.3e}$$
$$S_6 = C_{16} t^2 + C_{17} t + C_{18} \tag{16.3f}$$
$$S_7 = C_{19} t^2 + C_{20} t + C_{21} \tag{16.3g}$$
$$S_8 = C_{22} t^2 + C_{23} t + C_{24} \tag{16.3h}$$

With t in percentages of the chord. In order to make a best fit, a Matlab program was written to take the data and make a fit based on the least squares method. This resulted in numerical values for the coefficients C_1 through C_{24}. Table 16.1 displays the numerical values of these coefficients.

Coefficient	Value	Coefficient	Value
C_1	-0.008011	C_{13}	-3.371000
C_2	-0.000336	C_{14}	0.858039
C_3	0.000992	C_{15}	0.141600
C_4	0.013936	C_{16}	0
C_5	-0.003838	C_{17}	0
C_6	-0.000161	C_{18}	0
C_7	0.001243	C_{19}	7.201140
C_8	-0.009288	C_{20}	-0.676007
C_9	-0.002124	C_{21}	0.806629
C_{10}	0.012267	C_{22}	0.170454
C_{11}	-0.002398	C_{23}	-0.390563
C_{12}	-0.000274	C_{24}	0.101966

Table 16.1 The numerical values for the coefficients governing the lift algorithm.

The error introduced by this fitting procedure deserves special attention. As Fig. 16.9 indicates, the error under investigation here is the error between the data obtained through the CFD analysis and the data resulting from the fitted algorithm.

The fit error is defined as the square root of the sum of all the squared differences between the CFD and matched algorithm data, divided by the square root of the sum of the squared CFD data. In essence, the values of the differences between CFD and fitted data are used as components of a large $1 \times n$ vector. This vector is then normalized. The same is done with the coefficient values of the CFD data and the quotient between the two are a measure for the error made in the fit procedure:

$$\text{Fit error} = \frac{\text{norm}(\bar{C}_{l_{fit}} - \bar{C}_{l_{CFD}})}{\text{norm}(\bar{C}_{l_{CFD}})} \tag{16.4}$$

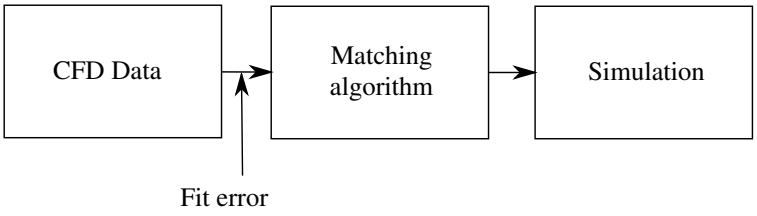

Fig. 16.9 A schematic representation of what the fit error encompasses.

For this fit this yielded an error of 5.5%. With the values C_1 through C_{24} known, the algorithm for the lift coefficient is known. The full equation for the lift algorithm is:

$$\begin{aligned} C_l = & [(C_1 t^2 + C_2 t + C_3)\kappa + (C_4 t^2 + C_5 t + C_6)]\alpha^3 \\ & + [(C_7 t^2 + C_8 t + C_9)\kappa + (C_{10} t^2 + C_{11} t + C_{12})]\alpha^2 \\ & + [(C_{13} t^2 + C_{14} t + C_{15})\kappa + (C_{16} t^2 + C_{17} t + C_{18})]\alpha \\ & + [(C_{19} t^2 + C_{20} t + C_{21})\kappa + (C_{22} t^2 + C_{23} t + C_{24})] \end{aligned} \tag{16.5}$$

To be more precise, it is known for a range of angles of attack from -20 to 20°. The simulation, however, also requires values for all the other angles of attack from -180 to -20° and from 20 to 180°. At these angles of attack, the flow is highly turbulent and a steady CFD analysis does not converge with residuals small enough to be considered reliable. Therefore, a more theoretical approach is taken in these ranges of angles of attack by assuming the aerodynamic properties to be close to that of a flat plate. From [13], for the range of angles of attack from -180 to -20° and from 20 to 180° we assume the lift coefficient to equal:

$$C_l = 3\cos^2(\alpha)\sin(\alpha) \tag{16.6}$$

With α in radians. For a numerical simulation it is imperative to create functions which are continuously differentiable. If they are not, numerical integration problems can occur which makes the simulation falter. Therefore, in order to continuously switch between the lift algorithm for low angles of attack (5) and equation (6) for high angles of attack, a step function is used to create a smooth transition.

For the drag and moment coefficients, a very similar method is used to obtain an algorithm which uses camber, airfoil thickness and angle of attack as an input and produces respectively a drag and a moment coefficient. At this point, the method is clear and it adds very little to repeat the same procedure twice more. The algorithm for drag yields:

$$C_d = [(C_{25}t + C_{26})\kappa^2 + (C_{27}t + C_{28})\kappa + (C_{29}t + C_{30})]\alpha^2 + [(C_{31}t + C_{32})\kappa + (C_{33}t^2 + C_{34}t + C_{35})] \quad (16.7)$$

With the numerical values for the coefficients:

Coefficient	Value	Coefficient	Value
C_{25}	0.546094	C_{31}	0.123685
C_{26}	0.022247	C_{32}	0.143755
C_{27}	-0.071462	C_{33}	0.495159
C_{38}	-0.006527	C_{34}	-0.105362
C_{29}	0.002733	C_{35}	0.033468
C_{23}	0.000686		

Table 16.2 The numerical values for the coefficients governing the drag algorithm.

For the moment algorithm, the fit operation yielded the following expression:

$$C_m = [(C_{36}t + C_{37})\kappa + (C_{38}t + C_{39})]\alpha + [(C_{40}t + C_{41})\kappa + (C_{40}t + C_{41})] \quad (16.8)$$

With the numerical values for the coefficients :

Coefficient	Value	Coefficient	Value
C_{36}	-0.284793	C_{40}	-1.787703
C_{37}	-0.026199	C_{41}	0.352443
C_{38}	-0.024060	C_{42}	-0.839323
C_{39}	-0.000559	C_{43}	0.137932

Table 16.3 The numerical values for the coefficients governing the moment algorithm.

With the coefficients C_1 through C_{43} known, the entire behavior of the aerodynamic forces as a function of angle of attack, airfoil thickness and camber are known. This approach allows for a modular simulation. One could quite easily apply the entire procedure with regard to a different airfoil and in the process obtain a different set of coefficients. Within the kite simulation toolbox, these different airfoil models can be selected. This approach allows the use of experimental data, as well as numerical data giving it added flexibility and new avenues of analysis.

16.4 Aerodynamic moment

In Sect. 16.3 it was shown that the lift and drag forces are introduced in the model as resultant forces on the nodes between the chordwise wire elements. Each vector

depicted in Fig. 16.3 is a fraction of the lift and drag vectors computed with the aforementioned fitting algorithm on each spanwise wing section. Adding the five fractions would yield the total resultant force vector for that particular sliver of wing. The aerodynamic moment of an airfoil is the result of the moment introduced by the changing pressure distributions on the upper and lower surface. This means that with changing angle of attack, airfoil thickness or camber, the five force fractions on the nodes change as well with respect to each other. This effect can be added to the simulation in a rather simple manner. Figure 16.10 shows a schematic view of a single airfoil as it is represented in the model.

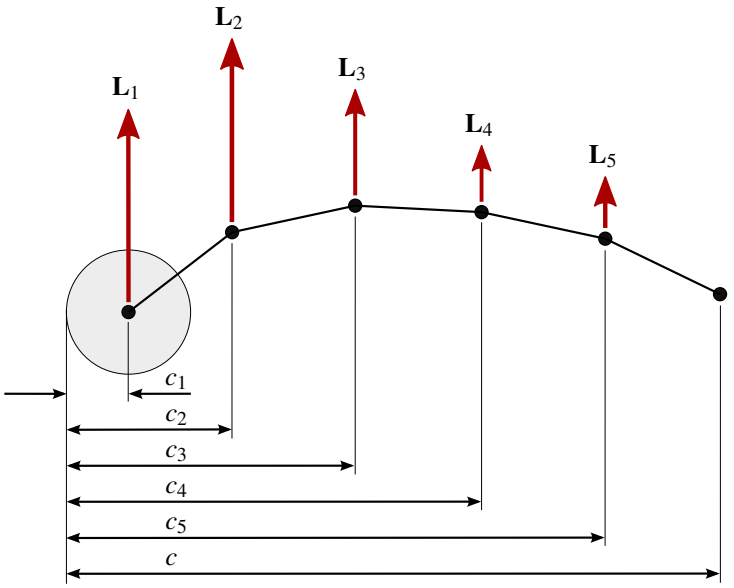

Fig. 16.10 A schematic representation of the airfoil model

For the lift we can write:

$$L = Lw_1 + Lw_2 + Lw_3 + Lw_4 + Lw_5 \tag{16.9}$$

With:

$$w_1 + w_2 + w_3 + w_4 + w_5 = 1 \tag{16.10}$$

Expanding on Eq. (16.9) we can also write:

$$\begin{aligned} L = {} & L(w_1 + u_1 a) + L(w_2 + u_2 a) + L(w_3 + u_3 a) \\ & + L(w_4 + u_4 a) + L(w_5 + u_5 a) \end{aligned} \tag{16.11}$$

With:

$$u_1 + u_2 + u_3 + u_4 + u_5 = 0 \tag{16.12}$$

And where "a" is an arbitrary increment of change. Its magnitude is dependent on the amount of change needed in the lift fractions to account for the changing aerodynamic moment of the airfoil. The aerodynamic moment is obtained from the moment algorithm derived in the previous section. It is therefore known for every combination of angle of attack, airfoil thickness and camber. This moment is taken around the quarter chord point of the airfoil. We can now write the following expression:

$$\begin{aligned} M = {} & L(w_1+u_1a)(0.25c-c_1)+L(w_2+u_2a)(0.25c-c_2) \\ & + L(w_3+u_3a)(0.25c-c_3)+L(w_4+u_4a)(0.25c-c_4) \\ & + L(w_5+u_5a)(0.25c-c_5) \end{aligned} \tag{16.13}$$

For a set of coefficients w_1 through w_5 and u_1 through u_5 which satisfy Eqns. (16.10) and (16.12) we can solve for the variable a.

$$a = \frac{M - L[0.25c - w_1c_1 - w_2c_2 - w_3c_3 - w_4c_4 - w_5c_5]}{-L[u_1c_1 + u_2c_2 + u_3c_3 + u_4c_4 + u_5c_5]} \tag{16.14}$$

In the simulation, the lift fractions can now be determined at every time step.

$$L_1 = L(w_1+u_1a) \tag{16.15a}$$
$$L_2 = L(w_2+u_2a) \tag{16.15b}$$
$$L_3 = L(w_3+u_3a) \tag{16.15c}$$
$$L_4 = L(w_4+u_4a) \tag{16.15d}$$
$$L_5 = L(w_5+u_5a) \tag{16.15e}$$

In this approach, only the lift force varied to incorporate the correct aerodynamic moment. In reality, due to the camber of the airfoil, the drag force fractions also introduce a moment with regard to the quarter chord point. However, the moment arm of the drag force is small compared to the moment arm of the lift force. Furthermore, the drag force itself is also significantly lower than the lift force. Therefore, the moment introduced by the drag force fractions is much smaller than the moment of the lift force fractions and therefore it has been neglected.

16.5 The toolbox methodology

Building these models by hand is extremely laborious and introduces a high chance of errors due to bad construction. Therefore, a toolbox was created to generate the model. The airfoil tool is a building block in a larger kite simulation toolbox. Three basic building blocks exist in this toolbox: An inflatable beam tool, a cable tool and an airfoil tool. Figure 16.11 shows the airfoil tool.

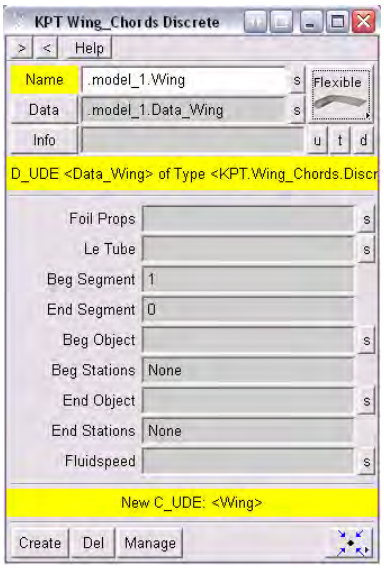

Fig. 16.11 The airfoil tool dialogue.

”Foil props” reverts to the data file containing the coefficients which govern the lift, drag and moment coefficients. This is where different airfoils can be selected in the simulation. It is therefore possible to have multiple wings with different airfoils operating within the same model. The airfoil model requires an inflatable beam as a base from which it is built. This is indicated in the field next to ”LE Tube”. ”Beg Segment” and ”End Segment” are indicators for the beginning and the end of the foil. ”Beg object” and ”End Object” indicate to what object the beginning and the end of the foil are attached. This could be another inflatable tube, a rigid rod or another foil. ”Beg Stations” and ”End Stations” indicate the specific markers on the objects where the foils are attached. For instance, the foil can be attached along the top of an inflatable strut or on the side of the strut. Lastly, ”Fluid speed” indicates which wind model the airfoil adheres to. For instance, a wind model which introduces a constant wind with increasing altitude or a wind model which introduces a steadily increasing wind as the kite gains altitude. The wind within the simulation is a separate module so that changing the wind properly affects all aspects of the simulation.

16.6 Comparison to existing experimental data

In this section the model is compared to existing wind tunnel tests on the basis of the shape and forces.

For the comparison, the measurements of [13] are used. Experimental data on single membrane airfoils is scarce and [13] was the only publication available. In

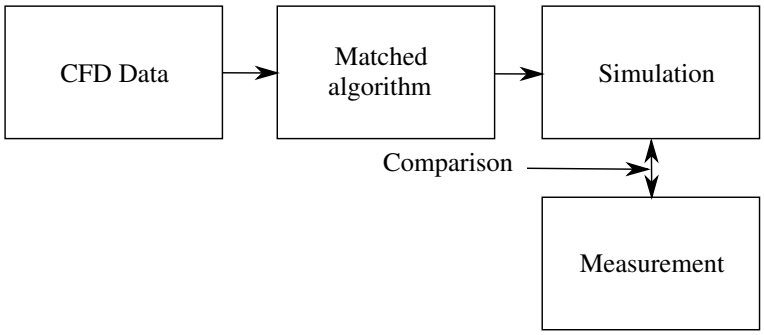

Fig. 16.12 A schematic representation of the model and comparison.

[13] a two-dimensional sail wing has been tested at different angles of attack and different values for slack of sail. The model consisted of a round metal bar with a fabric wrapped around it. The other end of the fabric was stretched backwards to create a sail wing. The airfoil of that wing had a 9.33% thickness. By rotating the bar, it was possible to add a slack of sail to the airfoil. For this comparison, only the results with no slack of sail are used for comparison since slack of sail is not included in the present simulation as such. In order to do a comparison, a model was created with the same dimensions and properties as the wind tunnel model of [13]. Figure 16.13 shows a comparison between measured and simulated lift coefficients at two different Reynolds Numbers (0.195×10^6 and 0.295×10^6).

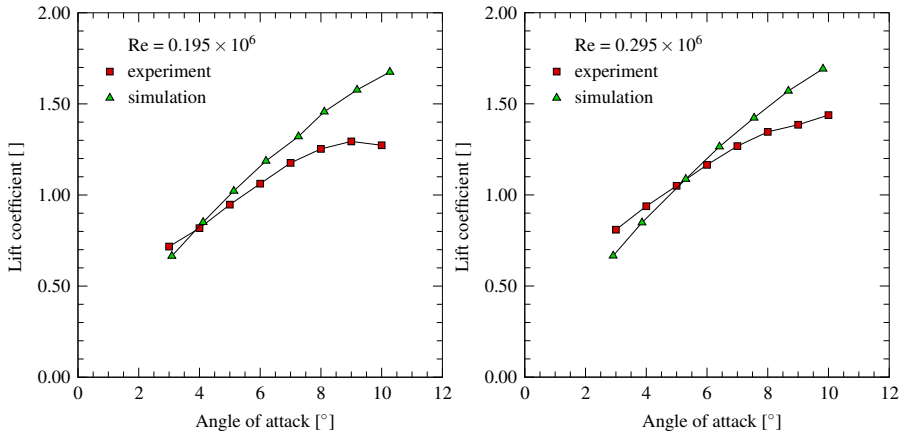

Fig. 16.13 Lift coefficient plots.

What becomes immediately apparent is that the simulation deviates from the measurements at higher angles of attack. In fact, in can be said that the simulation has a delayed stall behavior compared to the measurement. Most likely, this

is a direct effect of the CFD data used to build the lift coefficient algorithm. The CFD analysis is notorious for delayed stall and inaccurate drag predictions when significant turbulent flow is present. The single membrane airfoil has such a significant amount of turbulent flow, especially at higher angles of attack. At lower angles of attack, the values from the simulation closely correlate to the measured values. From this consideration, it is worth looking at a comparison between measured and simulated drag. A discrepancy is expected.

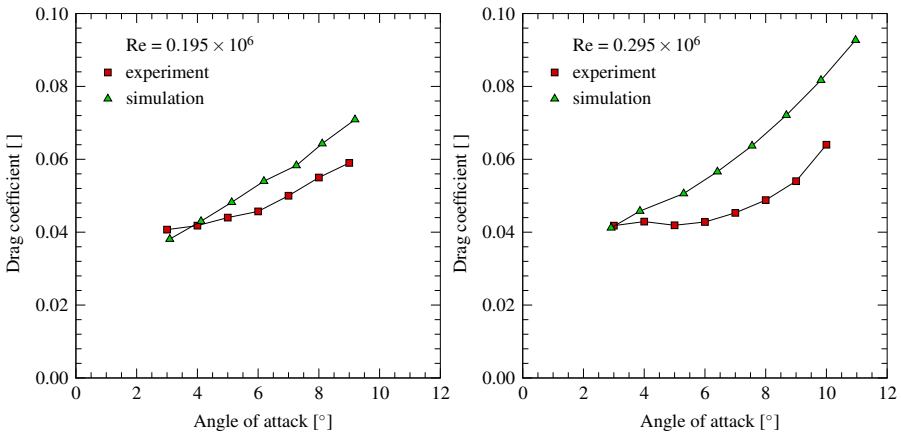

Fig. 16.14 Drag coefficient plots.

From Fig. 16.14 it can be seen that the simulation overestimates the amount of drag, especially for higher angles of attack. The interesting question is now whether or not this discrepancy is indeed the result of poor CFD results or whether it is the result of the simulation itself and the resulting shape of the airfoil. To evaluate this, the shapes of the measured and simulated airfoils are compared. [13] Gives the airfoil shapes for different values for the slack of sail. Only the plots with zero slack of sail are useful in this comparison. [13] Gives the shape of the airfoil for two Reynolds numbers ($Re = 0.195 \times 10^6$ and $Re = 0.295 \times 10^6$) at an angle of attack of 7°. At this angle of attack, the lift coefficients of both the measured and simulated airfoil are comparable. The question now is whether or not the airfoils have a comparable shape under this equal aerodynamic load. The conditions were simulated and a comparison was made.

Figure 16.15 was composed by overlaying the coordinates of the simulated airfoil onto the plot of the measured airfoil shape from [13]. It can be seen that the simulated and measured airfoil shapes are very close. This gives rise to the idea that the deviation between simulated and measured airfoil shapes at high angle of attack is the result of the data on which the aerodynamic coefficients are based.

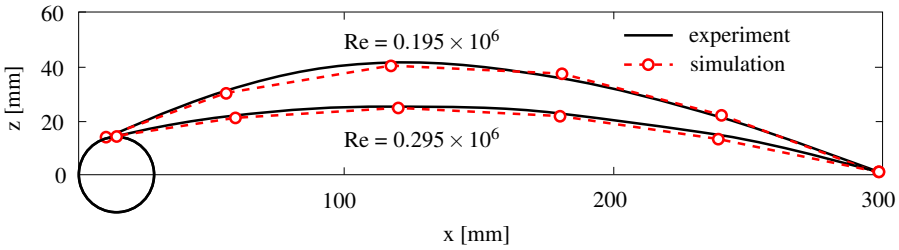

Fig. 16.15 Comparing measured and computed airfoil shapes at an angle of attack of 7°.

16.7 Conclusions and recommendations

Designers of kites and parafoils are interested in evaluating the general shape and the resulting forces of their wing designs. The simulation framework presented in this chapter provides an efficient and intuitive tool, which for most applications is sufficiently accurate. Models can be created with the toolkit in a matter of minutes and adaptations are easily incorporated and simulated. The simulation framework is based on a multibody system representation of the flexible wing. The lift-generating surface is partitioned into spanwise sections and chordwise line elements. This two-dimensional surface mesh is also used to apply the aerodynamic forces. It has been shown that, using a simple set of parameters, a good fit can be obtained within the regime indicated.

A comparison was performed with existing measured data [13]. The comparison showed good correlation of lift and drag at low angles of attack. At higher angles of attack, there exists a deviation which seems the result of a delayed stall behavior of the simulated wing. By comparing the shapes of the airfoil at low angles of attack, where the lift coefficients of the measured and simulated airfoil are comparable, it was shown that the shapes coincide well for the given value of angle of attack. A two-dimensional simulated wing experiencing a slowly increasing angle of attack closely represents the wing in the wind tunnel, both in shape and in resultant aerodynamic force. As the angle of attack increases, the measured wing stalls sooner than the simulated wing. It is most likely that at the reason for this discrepancy lies the CFD data on which the simulated aerodynamic force is based. More experimental data is required for further improvement of the fitted algorithm.

The simulation itself has proved to be a good approach to simulate the complexities of a flexible sail airfoil. Its modular character makes it easily expandable to create more complex three dimensional wings whilst maintaining a workable balance between accuracy and simulation speed.

Acknowledgements The authors would like to thank Filip Saad for assistance in the compilation of the manuscript.

References

1. Boer, R. G. den: Low speed aerodynamic characteristics of a two-dimensional sail wing with adjustable slack of the sail. Report LR-307, Delft University of Technology, Delft, Netherlands, 1980. http://resolver.tudelft.nl/uuid:18ae2cc6-434e-49c8-9296-d3fa450850a5
2. Boer, R. G. den: Numerical and experimental investigation of the aerodynamics of double membrane sailwing airfoil sections. LR-345, Delft University of Technology, Delft, Netherlands, 1982. http://resolver.tudelft.nl/uuid:d7b421a7-e1f4-4b3c-a053-969f5cab1920
3. Bosch, H. A.: Finite Element Analysis of a Kite for Power Generation. M.Sc.Thesis, Delft University of Technology, 2012. http://resolver.tudelft.nl/uuid:888fe64a-b101-438c-aa6f-8a0b34603f8e
4. Breukels, J.: An Engineering Methodology for Kite Design. Ph.D. Thesis, Delft University of Technology, 2011. http://resolver.tudelft.nl/uuid:cdece38a-1f13-47cc-b277-ed64fdda7cdf
5. Breukels, J., Ockels, W. J.: A Multi-Body System Approach to the Simulation of Flexible Membrane Airfoils. Aerotecnica Missili & Spazio **89**(3), 119–134 (2010). http://www.aerotecnica.eu/vol-89-n-3-september-2010/
6. Fink, M. P.: Full-scale investigation of the aerodynamic characteristics of a model employing a sailwing concept. Technical Report NASA TN D-4062, NASA Langley Research Center, Hampton, VA, USA, July 1967. http://hdl.handle.net/2027/uiug.30112106870097
7. Fink, M. P.: Full-scale investigation of the aerodynamic characteristics of a sailwing of aspect ratio 5.9. Technical Report NASA TN D-5047, NASA Langley Research Center, Hampton, VA, USA, Feb 1969
8. Maughmer, M. D.: A comparison of the aerodynamic characteristics of eight sailwing airfoil sections. In: Proceedings of the 3rd International Symposium on the Science and Technology of Low Speed and Motorless Flight, pp. 155–176, NASA Langley Research Center, Hampton, VA, USA, 29–30 Mar 1979
9. Nielsen, J. N.: Theory of Flexible Aerodynamic Surfaces. Journal of Applied Mechanics **30**(3), 435–442 (1963). doi: 10.1115/1.3636575
10. Ockels, W. J., Lansdorp, B., Ruiterkamp, R.: Ship Propulsion by Kites Combining Energy Production by Laddermill Principle and Direct Kite Propulsion. In: Proceedings of the Kite Sailing Symposium, Seattle, WA, USA, 28–30 Sept 2006. http://resolver.tudelft.nl/uuid:00730203-1f6b-4881-b6d7-e0aca6b4f545
11. Ockels, W. J.: Laddermill, a novel concept to exploit the energy in the airspace. Journal of Aircraft Design **4**(2-3), 81–97 (2001). doi: 10.1016/s1369-8869(01)00002-7
12. Ormiston, R. A.: Theoretical and Experimental Aerodynamics of the Sailwing. Journal of Aircraft **8**(2), 77–84 (1971). doi: 10.2514/3.44232
13. Spierenburg, G. J.: Continued Development and Experimental Validation of a Kite Design and Simulation Tool. M.Sc.Thesis, Delft University of Technology, 2005
14. Sweeney, T. E.: Exploratory Sail Wing Research at Princeton. Technical Report 578, Princeton University, NJ, USA, Dec 1961. http://handle.dtic.mil/100.2/AD0275307
15. Thwaites, B.: The Aerodynamic Theory of Sails. I. Two-Dimensional Sails. Proceedings of the Royal Society of London. Series A. Mathematical and Physical Sciences **261**(1306), 402–422 (1961). doi: 10.1098/rspa.1961.0086